J Solid State Electrochem (2010) 14:157–166
DOI 10.1007/s10008-009-0801-x

ORIGINAL PAPER

$NiCr_xFe_{2-x}O_4$ as cathode materials for electrochemical reduction of NO_x

F. Bræstrup · K. K. Hansen

Received: 5 November 2008 / Revised: 28 January 2009 / Accepted: 28 January 2009 / Published online: 25 February 2009

Abstract Solid solutions of spinel-type oxides with the composition $NiCr_xFe_{2-x}O_4$ ($x = 0.0, 0.5, 1.0, 1.5, 2.0$) were prepared with the glycine–nitrate combustion synthesis. Four-point DC resistivity measurements show an increase in the conductivity as more Cr is introduced into the structure, whereas dilatometer measurements show that the linear thermal expansion decreases with increasing Cr content. The oxides were used as electrode materials in a pseudo-three-electrode setup in the temperature range of 300–600 °C. Cyclic voltammetry and electrochemical impedance spectroscopy were used to characterize the electrochemical behavior in 1% NO, 1% NO_2, and 10% O_2. $NiCr_2O_4$ shows high activity in NO and NO_2 relative to O_2 and can therefore be considered as a possible electrode material. Peaks were detected in the voltammograms recorded on $NiCr_2O_4$ in 1% NO. The origin of the peaks seems to be related to the oxidation of Cr or the formation of nitrogen-containing species formed on the surface of the electrode.

Keywords Spinel-type oxide · Conductivity · Powder diffraction · NO_x · O_2

F. Bræstrup (✉) · K. K. Hansen
Fuel Cells and Solid State Chemistry Division,
Risø National Laboratory for Sustainable Energy,
Technical University of Denmark,
Copenhagen, Denmark
e-mail: frantz.braestrup@risoe.dk

Introduction

The formation of NO and NO_2 gases is one of the main polluting agents from internal combustion processes in diesel fired engines. In addition to being harmful to human health [1], NO_x also contributes to the formation of acid rain [2]. Over the years, scientists have been working on solving the problem with NO_x emission, and so far, the selective catalytic reduction process (SCR) has gained the most attention for diesel exhaust. In SCR, the reduction of NO_x is performed by injecting a reducing agent, such as ammonia, urea, or a hydrocarbon, into the exhaust gas upstream of the SCR catalyst.

An alternative way of solving the problem with NO_x emission is an electrochemical reduction of NO_x over a solid state cell [3]. In such a cell, NO_x gases are reduced at the cathode while O_2 is formed at the anode. However, since O_2 is also present in relatively high concentrations in the exhaust gas from a diesel fired engine, it can also be reduced at the cathode, which will lead to a high consumption of current. A good electrode material therefore has to be selective towards reduction of NO_x.

Pd, Pt, Au, Ag, and Ir have previously been tested [3–7] as possible electrode materials, and a few of them have also shown some interesting results; however, most of the metals are relatively expensive, which has intensified the research for low-cost ceramics to be used as electrode materials. NiO and RuO_2 have also been suggested as candidates for electrochemical NO_x removal [5, 8, 9]; however, in the case of RuO_2, Ru is highly poisonous and forms volatile higher oxides such as RuO_3 and RuO_4. In the case of NiO, operation temperatures have been shown to be too high compared with the temperature of the exhaust gas from a

diesel engine. Different perovskites [10–13] and individual members of the Ruddleston–Popper phases [14] have also been reported as possible electrode materials; however, current densities are relatively low and the activity in O_2 is high compared to the activity in NO. Catalytic NO_x decomposition on spinel-type oxides [15–21] has been reported; however, only a few observations on electrochemical decomposition on spinel-type electrode materials [22–24] have been presented in literature to our knowledge.

$NiCr_2O_4$ has been analyzed as a possible sensor material [25–27] to detect NO_x gases in the presence of O_2. It has shown high selectivity towards detection of NO_x and no cross selectivity towards CO_2. In this study, the electrochemical reduction of NO_x and O_2 has been investigated on spinel-type oxides, $NiCr_xFe_{2-x}O_4$ ($x = 0.0, 0.5, 1.0, 1.5, 2.0$), with the purpose of finding cheap electrode materials, of nonprecious metals, to be used in electrochemical filters.

The spinel-type oxides were measured in a pseudo-three-electrode setup [28] suggested by Fabry [29]. The advantage with this setup is to suppress the effect of microstructures such as porosity, grain size, and grain shape. Recorded data will therefore reflect the true electro-catalytic properties of the material. However, using a cone-shaped point electrode will not make it possible to measure any gas conversion because of the small contact area (compared to the flow rate).

Experimental details

Sample preparation and X-ray diffraction

$NiCr_xFe_{2-x}O_4$ ($x = 0.0, 0.5, 1.0, 1.5, 2.0$) were prepared from aqueous metal-nitrates ($Ni(NO_3)_2$, $Cr(NO_3)_3$ and $Fe(NO_3)_3$) using the glycine–nitrate combustion synthesis [30]. After synthesis, the powder was ball milled for 24 h and then calcined in air at 1,000 °C for 6 h. All samples were analyzed by X-ray diffraction using a STOE theta-theta diffractometer. Scans were conducted over the 2θ-range of 15°–80°, with a step width of 0.05°. Le Bail fits were carried out using the program Jana2000 [31] in order to determine the unit cell parameter, a. Pseudo-Voigt profile functions were used, and the background was modeled with a 10 terms Legendre polynomials.

The powder was pressed uniaxially at 1 ton into pellets, followed by isostatic pressing at 50 tons. This was done in order to make the pellets more dense and to increase their mechanical strength. The samples were then sintered in air at 1,000 °C for 6 h. The pellets were then mechanically tooled into identical cone-shaped electrodes [11, 32] and bares of $4 \times 4 \times 16$ mm. The densities of the samples were measured by the Archimedes principle (see Table 1).

Dilatometry

The linear thermal expansion was measured by dilatometry in air (flow rate: 50 ml/min) using a NETZSCH DIL 402C dilatometer with a sample load of 30,000 cN. The sample-rod was heated from room temperature up to 1,000 °C and back at 2 °C/min. The sample remained at 1,000 °C for 2 h. Data were calibrated to an Al_2O_3 standard at identical conditions.

Four-point DC resistivity measurements

Four-point DC resistivity measurements were conducted on sintered elongated bars. Two Pt wires were attached onto the bars with Pt paste and data were recorded with an in-house data acquisition software, ELCHEMEA. The resistivity was measured every 5 min from room temperature to 1,000 °C and back again with a ramp rate of 2 °C/min and a 2-h dwell at every 50 °C interval. The densities of the elongated rods were measured by the Archimedes principle, and the resistivities of the samples were then corrected for the porosity using the Bruggeman asymmetric model [33].

Cyclic voltammetry and impedance spectroscopy

Cyclic voltammetry (CV) and electrochemical impedance spectroscopy (EIS) were recorded with a

Table 1 Electrode porosities; Curie temperatures, T_c; and expansion coefficients, α

Compound	Porosities	T_c	α
$NiFe_2O_4$	12.5 %	584 °C	$8.0(2) \cdot 10^{-6}$ °C^{-1}
$NiCr_{0.5}Fe_{1.5}O_4$	5.8 %	423 °C	$4.6(1) \cdot 10^{-6}$ °C^{-1}
$NiCrFeO_4$	13.7 %	284 °C	$2.3(1) \cdot 10^{-6}$ °C^{-1}
$NiCr_{1.5}Fe_{0.5}O_4$	8.4 %	~130 °C	$4.1(1) \cdot 10^{-6}$ °C^{-1}
$NiCr_2O_4$	3.6 %	–	$5.6(3) \cdot 10^{-7}$ °C^{-1}

The expansion coefficients are mean values calculated from 600–800 °C. Curie temperatures were read of the graphs and, therefore, statistical errors are given

Gamry Femtostate in a pseudo-three-electrode setup. The cone, acting as a point electrode, was arranged with the tip placed downwards on a polished one-end closed yttrium-stabilized-zirconia-tube electrolyte containing air as reference gas and a silver electrode used as the counter/reference electrode. CV and EIS were recorded in the temperature range from 300 to 600 °C, with a 100 °C step. Data were recorded in 10% O_2 in Ar, 1% NO in Ar, or 1% NO_2 in Ar (Air Liquide) with a flow rate of 20 ml/min. Measurements containing NO_2 gas were performed only at 300 and 400 °C. A 1-h equilibrium time was used to record the open circuit voltage before recording the voltammograms in the potential range of −0.6–0.6 V with different sweep rates (1.0, 10, 100, 200, 400, and 600 mVs^{-1}). EIS were recorded from 177,793(1) to 0.050(1) Hz with 10 points/decade and an amplitude of 24 mV (rms). In order to compare the electrodes directly, the current recorded in the voltammograms (typically in the order of 10^{-8}–10^{-7} A at 500 °C, −0.6 V) were converted into current densities by dividing with the contact area, which was determined by EIS using Newman's formula [34], Eq. 1,

$$r = \frac{1}{4\sigma R_e}, \tag{1}$$

where r is the radius of the circular contact area, σ is the specific conductivity of the electrolyte material, and R_e is the electrolyte resistance. σ can be determined from Eq. 2 [35].

$$\sigma = \frac{1.51 \cdot 10^6}{T} \cdot e^{\frac{-0.94[eV]}{Tk_B}}, \tag{2}$$

where T and k_B are the temperature and the Boltzman's constant, respectively. Uncertainties on the contact areas were less than 6%. No corrections were made for the IR drop since calculations showed that the corrections were less than 0.2% at all temperatures.

Results and discussions

X-ray diffraction

Almost all materials were single-phase cubic spinel-type oxides. However, a small impurity phase of tetragonal $NiCr_2O_4$ (approx. 5%) was detected together with the cubic $NiCr_2O_4$. $NiFe_2O_4$ has an inverse spinel-type structure with Ni^{2+} located primarily on the octahedral sites and Fe^{3+} located on both the tetrahedral and the octahedral sites. The ionic radii of Ni^{2+} on tetrahedral and octahedral sites are 0.55 and 0.69 Å, respectively, whereas Fe^{3+} has an ionic radius of 0.63 Å (tetrahedral coordinations) or 0.65 Å (octahedral coordinations) [36]. When Cr^{3+}, having an ionic radius of 0.62 Å (octahedral coordinations), is introduced in the structure in favor of Fe^{3+}, it will enter the octahedral lattice site [37], keeping the structure inverse as long as $x \leq 1$. When $x > 1$, Ni is forced to leave the octahedral sites and move to a tetrahedral site, which causes a shrinkage of the unit cell because of the different ionic radii of Fe and Ni. Replacing more Fe with Cr, the structure will now change towards a normal spinel structure [38]. X-ray diffraction measured at room temperature show an decrease in unit cell parameters with increasing Cr content (Fig. 1). A relatively large change of the unit cell parameter is observed when half of the Fe has been replaced by Cr. We would have expected a larger unit cell in the case of $NiCrFeO_4$; however, one explanation would be that a relatively large amount of the Ni^{2+} is located on the tetrahedral sites where its ionic radius is smaller relative to Fe^{3+}.

Conductivity measurements

Figure 2 shows the specific conductivity of the spinels as a function of temperature. Below ~ 650 °C, the conductivity decreases slightly when Cr^{3+} is introduced in the lattice. The conductivity then increases as more Cr^{3+} is incorporated into the lattice, with $NiCr_2O_4$ having the highest conductivity. The conductivity of $NiFe_2O_4$ is mainly attributed to the cation–anion–cation indirect interactions between octahedral sites, where the transport property rises from hopping of localized d electrons between cations [39, 40]. When Cr^{3+} is introduced into the structure, it tends to shield this interac-

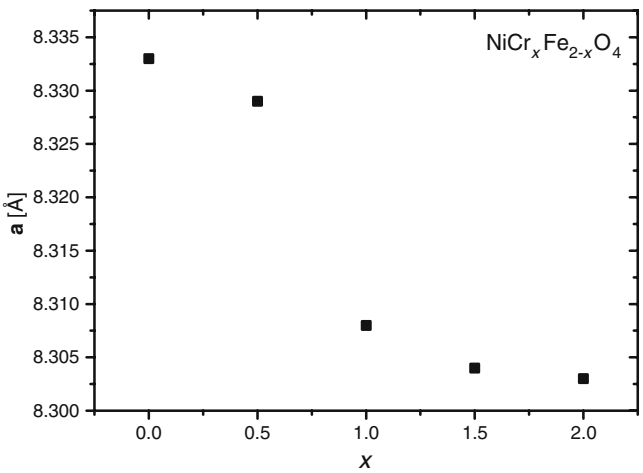

Fig. 1 Unit cell parameters, a, measured at different spinel compositions. A small decrease in a is observed. *Error bars* are at the same magnitude as the dimension of the points

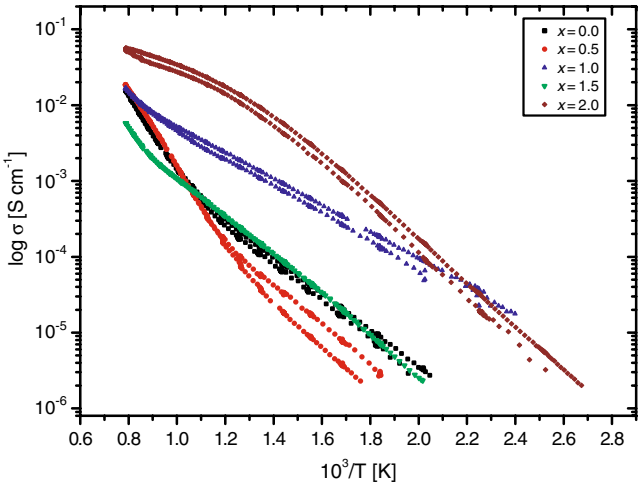

Fig. 2 Four-point DC conductivity measurements of the spinels measured from room temperature to 1,000 °C in air. *x* refers to the Cr content

tion mechanism and thereby decrease the conductivity. However, as more Cr^{3+} is introduced into the structure, the unit cell decreases, and so does the Cr^{3+}–Cr^{3+} distance. This will strengthen the direct interaction between the Cr^{3+} ions and eventually be the dominating interaction mechanism in the spinel [41]. This interaction will cause an increase in the conductivity at high temperatures, as also observed in Fig. 2.

Dilatometry

Measurements with dilatometry show a gradual decrease in the relative linear expansion (see Fig. 3) as more Cr is incorporated into the structure. The thermal expansion coefficients, α, defined as $\alpha = \frac{1}{L}\frac{\delta L}{\delta T}$, for the different compounds are shown in Table 1. For most of the samples, the Curie temperature, T_c, can be detected as a relatively narrow and asymmetrical peak in the graph of thermal expansion coefficients [42]. T_c decreases with increasing Cr content (see Table 1), which was also reported by Rais [43].

For most of the spinels, the relative linear expansion reveals an almost reversible discontinuity (see Fig. 4) at around 700–900 °C, all appearing during the heating and the cooling stage. This suggests a redistribution between cations on tetrahedral and octahedral sites. In most cases, the compounds are not in equilibrium at low temperatures where the ordering of the cations is controlled by the kinetics [44]. At high temperatures, the spinels are in equilibrium with respect to the cation order–disorder, reflecting the thermodynamic drive towards high-temperature disorder. When the cation rearrangement has reached equilibrium, the thermal expansion takes over the main process, which causes a decrease of the relative linear expansion. Similar observations have been reported on other ferric-spinels [24].

The oxygen ion conductivity of spinels is very low [45, 46]. Therefore, in order to measure any gas conversion, the number of three-phase boundaries must be increased. A mixed electrode of spinel and, for instance, $Ce_{0.9}Gd_{0.1}O_{1.95}$ (CGO10) (an oxygen ion conductor) is therefore needed. Results show that the thermal expansion coefficient of the spinels is, in general, smaller than the thermal expansion coefficient of CGO10 ($\alpha = 11.9 \cdot 10^{-6}$ °C^{-1} [47]). A mixed electrode manufactured with one of our spinels and CGO10 would therefore be a disadvantage because of the large difference in expansion

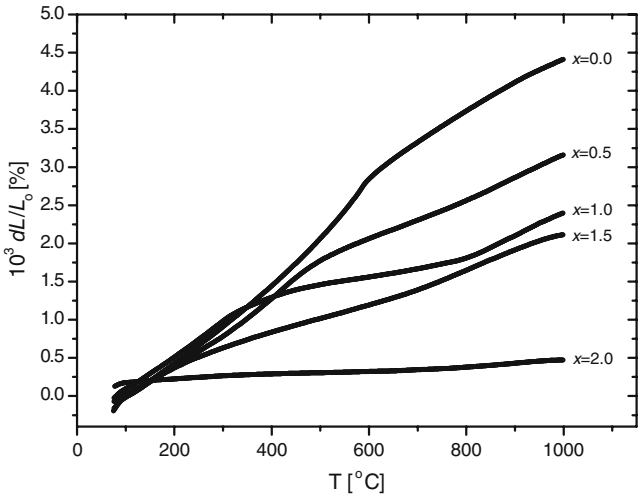

Fig. 3 Linear expansion of the different spinels measured in the temperature range of 80 to 1,000 °C. *x* refers to the Cr content

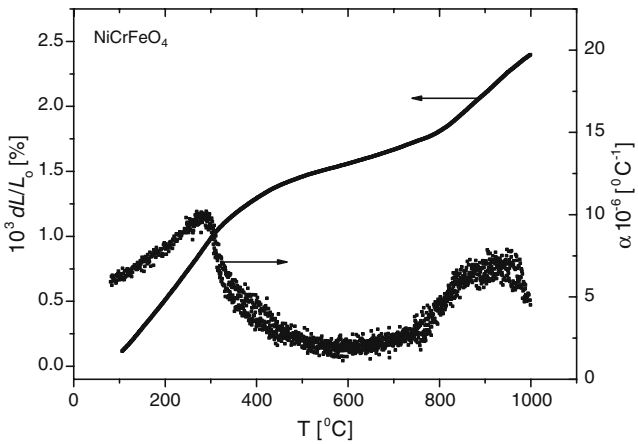

Fig. 4 Linear expansion and the expansion coefficient recorded on the $NiCrFeO_4$ electrode. The Curie temperature can easily be detected at ~ 284 °C

coefficients. A small particle size and a high porosity could maybe reduce tensions in the microstructure, but experiments must be made in order to verify this.

Cyclic voltammetry

Part of the voltammograms recorded at 300, 400, and 500 °C in 1% NO are shown in Fig. 5. The highest activity is recorded for $NiFe_2O_4$, but when Cr^{3+} is introduced into the structure, a gradual decrease of the activity is detected. A small increase in activity is seen when all Fe^{3+} have been substituted by Cr^{3+}, and it suggests that Fe^{3+} is more electrocatalytically active than Cr^{3+} in NO.

Figure 6 shows three voltammograms recorded on $NiCr_2O_4$ in 1% NO_2 at 400 °C. At high sweep rates, the voltammograms appear as straight lines in the potential range, and only at 1 or 10 mV s^{-1}, a small curvature is observed at maximum and minimum applied potential. Voltammograms recorded at 300 °C are similar to the one recorded at 400 °C, although the I/E curves are linear at all sweep rates. The linearity seems to be caused by limitations of the ionic conductivity in the electrolyte. It is not clear why the activity of the $NiCr_{1.5}Fe_{0.5}O_4$ electrode is much lower than the other materials. Measurements were repeated several times but with the same result. Analyzing the current densities of the spinels shows that the activities in O_2 and NO (see Fig. 7) change only little (not including $NiFe_2O_4$); however, current densities in NO_2 seem to vary in a nonsystematic way at 300 °C as a function of the Cr content. At 400 °C, current densities in NO_2 seem more stable through the series until no more Fe is left in the structure. Then, the current density on the $NiCr_2O_4$ electrode changes significantly. The same picture is seen in NO and O_2; however, this time, it is the second end member of the series, $NiFe_2O_4$, that shows the largest activities, whereas the Cr-containing spinels show lower activities. The cathodic activity in O_2 is, in general, quite low at all temperatures, which is an advantage since it will minimize the extra consumption of current caused by the reduction of O_2 in the exhaust gas from a diesel engine (see "Introduction"). The porosities of the electrodes were, in general, low and relatively similar in values. They were therefore not taken further into account.

Because of the small contact area and the relatively high flow rate, no direct gas conversion could be measured. Therefore, in order to evaluate the compounds as possible electrode materials, current ratios between NO_x and O_2 were used as a relative tool to give information of which spinels there should be tested further.

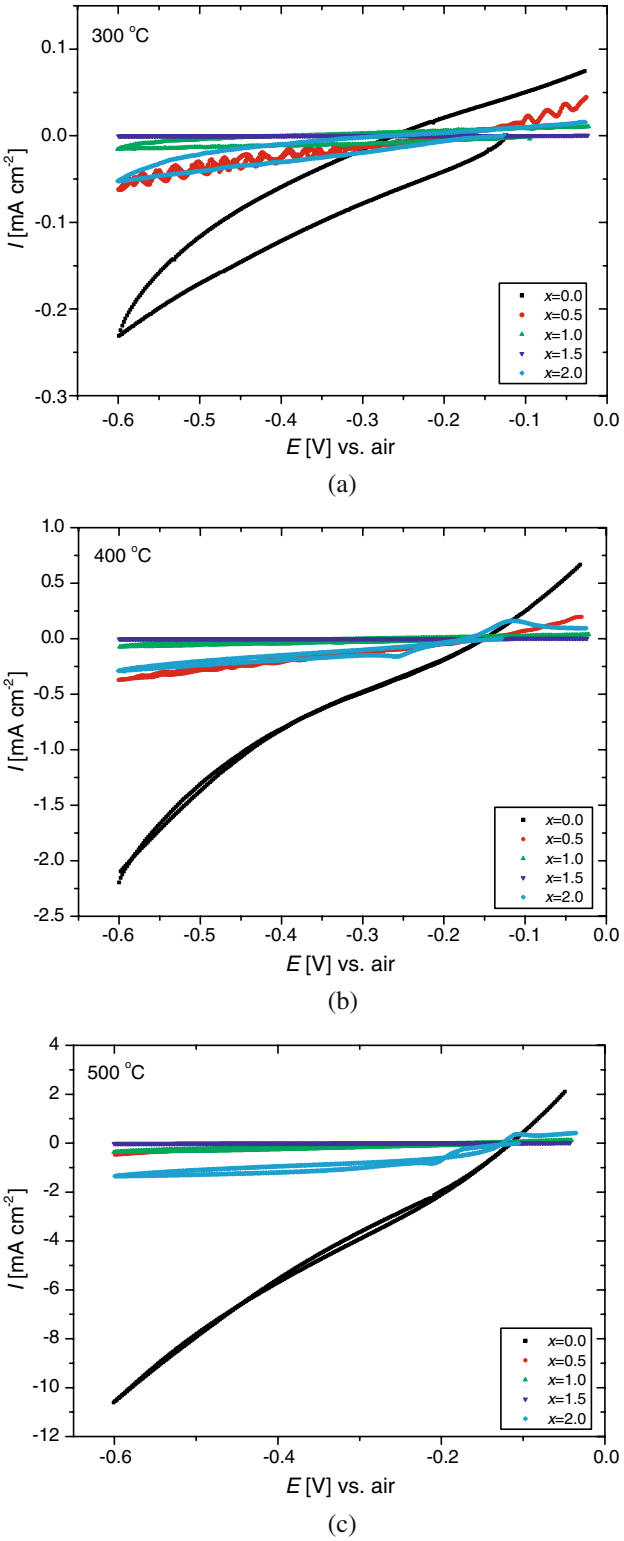

Fig. 5 Cyclic voltammograms on $NiCr_xFe_{2-x}O_4$. **a–c** Part of the voltammograms (−0.6–0 V) recorded at 300, 400, and 500 °C, respectively. The voltammograms were recorded in 1% NO with air as reference gas (sweep rate: 1 mV s^{-1}). The more "wave-shaped" curve of $NiCr_{0.5}Fe_{1.5}O_4$ recorded at 300 °C is due to noise, which reflects a small measured current that again originates from a very small contact area between the cone-shaped electrode and the electrolyte

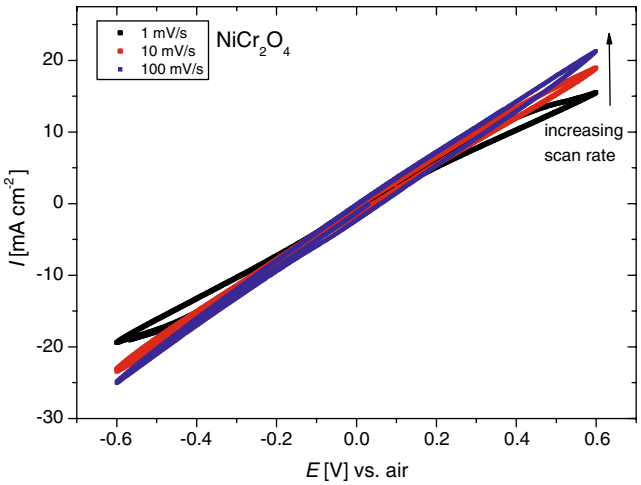

Fig. 6 CV on $NiCr_2O_4$ at 400 °C. Data were recorded in 1% NO_2. Only voltammograms recorded with sweep rates of 1, 10, and 100 mV s^{-1} are shown

Figure 8 shows the ratio of the current densities with respect to O_2 (I_{NO}/I_{O_2}). $NiCr_2O_4$ has the highest ratio, which decreases with increasing temperature. $NiFe_2O_4$ and $NiCr_{0.5}Fe_{1.5}O_4$ also show relatively high current ratios; however, this is only at 300 °C, and in the case of $NiCr_{0.5}Fe_{1.5}O_4$, also at 400 °C. The much lower current ratio of $NiFe_2O_4$ at 400 °C seems to be the result of the relatively high activity in O_2 at temperatures above 300 °C (see Fig. 7).

Figure 9 shows the current ratios, I_{NO_2}/I_{O_2}, of NO_2 with respect to O_2 at −0.6 V. All electrode materials, except for $NiCr_{1.5}Fe_{0.5}O_4$, show much higher activity in NO_2 compared to NO and O_2. $NiCr_2O_4$ shows significantly higher current ratios from 600 to 700, which seems to be a result of the relatively low activity in O_2.

A general problem when working with cone-shaped electrodes is the ohmic drop across the electrode. If the conductivity of the electrode is very low compared to the ionic conductivity of the electrolyte, Newman's formula (Eq. 1) will give inaccurate contact areas. In our case, the high-frequency interception with the real axis in the impedance plot will be given by Eq. 3:

$$R_s = R_e + R_c, \tag{3}$$

where R_c is the ohmic resistivity of the cone-shaped electrode. If $R_e \gg R_c$, R_e can be taken as equal to R_s, which is then used in Newman's formula to calculate the contact areas. Knowing the specific conductivity of the electrode material, finite-element calculations, using the software program COMSOL 3.4 Multiphysics [48], can be applied to calculate the resistance of the cone. However, results show that the area correction is less than 5% at 600 °C, and therefore, a correction of R_s is not needed.

Peaks in voltammograms

Peaks were detected on the voltammograms recorded in the NO atmosphere using the $NiCr_2O_4$-electrode (see Table 2). Peaks were not detected in O_2 and NO_2, however, since the activity in NO_2 is 10 times higher compared to NO, which might explain why no peaks are detected on the $NiCr_2O_4$ electrode. Figure 10 shows the cyclic voltammograms recorded on $NiCr_2O_4$ at 500 °C with increasing sweep rates. Voltammograms recorded at 400 °C and 600 °C look similar to the one recorded at 500 °C and are therefore not presented. Voltammograms recorded at 300 °C are smeared out when sweep rates exceed 10 mV s^{-1}. This is caused by limitations of the electronic conductivity in the electrode and the ionic conductivity in the electrolyte.

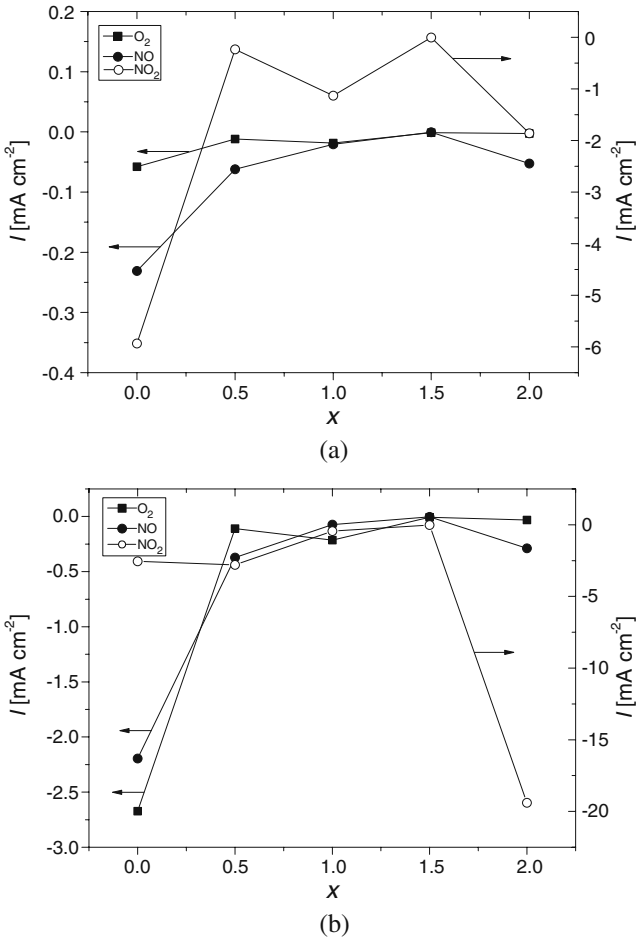

Fig. 7 Current densities recorded on $NiCr_xFe_{2-x}O_4$ at **a** 300 °C and **b** 400 °C with an applied potential of −0.6 V. *x* refers to the Cr content

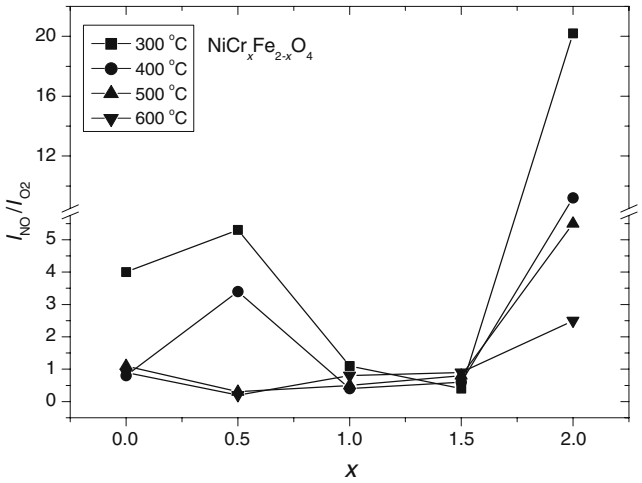

Fig. 8 Current ratios between NO and O_2 for the different spinels ($NiCr_xFe_{2-x}O_4$). $NiCr_2O_4$ shows higher current ratios compared to the other spinels. x refers to the Cr content

Two oxidation (and reduction) peaks positioned very close to each other are observed at high sweep rates (200–600 mV s^{-1}) at 500 and 600 °C. The smaller oxidation peak is most detectable after the second cycle. The larger reduction/oxidation peaks shift (see Fig. 11) approximately 20 mV towards lower potentials after the second cycle. The peaks does not reflect a complete reversible reaction because $|I_{red}/I_{ox}| \neq 1$. The origin of the peaks is not understood completely; however, speculations can be made: Since no peaks were observed in O_2 or in NO_2, an obvious conclusion would be to assign at least one set of peaks to the reduction/oxidation of NO as shown in Eqs. 4 and 5,

$$4e^- + 2NO \rightarrow N_2 + 2O^{2-}, \tag{4}$$

$$2O^{2-} + 2NO \rightarrow 2NO_2 + 4e^-. \tag{5}$$

We would not expect the reverse reaction of Eq. 4 because of the high electrochemical stability of N_2. In order to verify that the peaks are related to the reduction/oxidation of NO, the peak heights of the larger oxidation peak were plotted vs the square root of the sweep rate (see Fig. 12). A linear trend line is observed at 400, 500, and 600 °C; however, at high sweep rates at 600 °C, a deviation from the linear trend is observed. This is caused by the interference with the peak at slightly lower potential. Using Eq. 6 [49]:

$$\frac{i_p}{A} = 0.4463F\sqrt{\frac{F}{RT}}c^*\sqrt{\nu}\sqrt{D_a}, \tag{6}$$

where i_p is the peak height, A is the contact area, F is the Faraday constant, c^* is the initial concentration of the active species, ν is the sweep rate, and D_a is the apparent diffusion constant. The diffusion constant calculated in 1% NO at 500 °C is equal to $2.3 \cdot 10^{-13}$ m^2 s^{-1}. The diffusion constant of a perfect gas (kinetic theory of a perfect gas [50]) is equal to

$$D = \frac{1}{3}\lambda\bar{c}, \tag{7}$$

where λ is the mean free path, given as:

$$\lambda = \frac{K_B T}{\sqrt{2}\sigma p}, \tag{8}$$

and $\bar{c}$ is the mean speed, given as:

$$\bar{c} = \sqrt{\frac{8RT}{\pi M}}. \tag{9}$$

σ is the collision cross-section, p is the pressure, R is the gas constant, and M is molar mass. Calculations show that, for a perfect gas (1% NO), $D = 4.1 \cdot 10^{-4}$ m^2 s^{-1} (500 °C), which is much larger than the measured value. This suggests that the origin of the peak or peaks might be coupled to a bulk diffusion.

Within the potential range, two electrochemical reactions can occur, as shown in Eqs. 10 and 11:

$$\frac{1}{2}O_2 + NiCr_2O_4 \rightarrow NiO + 2CrO_2 \quad E = -0.14\,V, \tag{10}$$

$$\frac{3}{2}O_2 + NiCr_2O_4 \rightarrow NiO + 2CrO_3 \quad E = -0.28\,V. \tag{11}$$

The equilibrium potentials are calculated at 500 °C using FactSage 5.5 [51]. The position of the reduction and oxidation peaks at 400 and 500 °C (1 mV s^{-1})

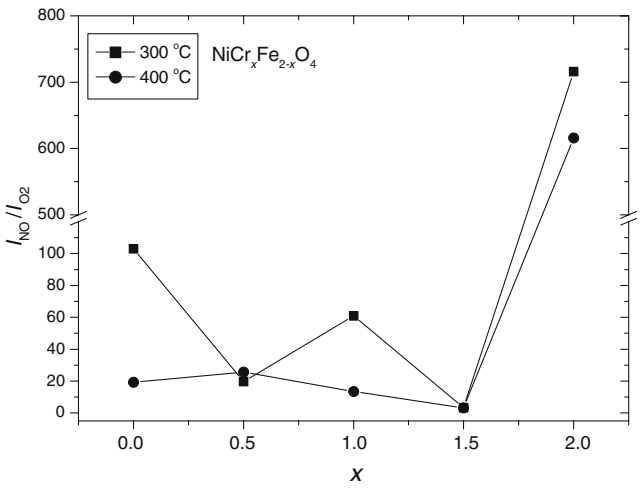

Fig. 9 Current ratios between NO_2 and O_2 for the different spinels ($NiCr_xFe_{2-x}O_4$). $NiCr_2O_4$ shows higher current ratios compared to the other spinels. x refers to the Cr content

Table 2 Positions of the oxidation (Ox) and reduction (Re) peaks found for $NiCr_2O_4$

Sweep rate	400 °C		500 °C		600 °C	
–	Ox	Re	Ox	Re	Ox	Re
1 mVs^{-1}	−111 mV	−261 mV	−102 mV	−212 mV	−80 mV	−194 mV
10 mVs^{-1}	−55 mV	−306 mV	−85 mV	−242 mV	−68 mV	−224 mV
100 mVs^{-1}	34 mV	–	−15 mV	−304 mV	−37 mV	−264 mV
200 mVs^{-1}	64 mV	–	15 mV	−324 mV	−18 mV	−284 mV
400 mVs^{-1}	91 mV	–	42 mV	−422 mV	3 mV	−318 mV
600 mVs^{-1}	114 mV	–	65 mV	−455 mV	18 mV	−361 mV

The position of the reduction peak could not be determined for all sweep rates at 400 °C. All positions were read of the graphs and therefore no statistical errors are given

matches quite well with the equilibrium potential of Eq. 10; however, the position of the peaks at 600 °C does not coincide well with the equilibrium potential of Eq. 10. The oxidation peak seems to be shifted and approximately 50 mV more towards high potentials than expected. Formation of CrO_3 seems, however, not to be present due to the position of the peaks. Considering the charge transfer and assuming a perfect cone shows that the reaction 10 proceeded approximately 19 μm up in the cone electrode (500 °C, 1 mV s^{-1}). If the oxidation/reduction of Cr is in fact the explanation of the peaks, we are still left with the questions of why no peaks are observed in O_2 or NO_2, why no voltammograms of the other Cr-containing spinels appear to show peaks in any of the gases, what causes the second reduction/oxidation peak, and finally why we start by seeing a reduction peak when no CrO_2 could be detected by X-ray diffraction before starting the experiment.

Since no peaks were detected in the O_2-containing atmosphere for $NiCr_2O_4$, it suggests that the origin of the peaks is not due to the formation of Cr oxides but must be found in the formation of other unknown nitrogen-containing species on the surface. Similar observations were reported by Simonsen [22], and peak formations were also attributed to the formation of nitrogen-containing species on the surface. Earlier reports show that Cr species evaporate relatively easy at elevated temperatures [52, 53], and it is possible that some of the Cr in the outermost atomic layers of the particles has evaporated during sintering. This would lead to a depletion of Cr at the surface of the materials and would explain the absence of peaks in the Fe-containing materials since it has been shielded from contact with any of the reaction gases. The second set of peaks is very difficult to ascribe a certain process, but it may be due to reduction/oxidation processes of the NO gas. Therefore, giving the missing peaks in O_2 on the $NiCr_2O_4$ electrode suggests the formation of other (unknown) stable or metastable nitrogen-containing species on the surface of the electrode. However, it cannot be $Ni(NO_3)_2$ or $Cr(NO_3)_3$ since they will decompose above 300 °C [54, 55]. The position of the peaks

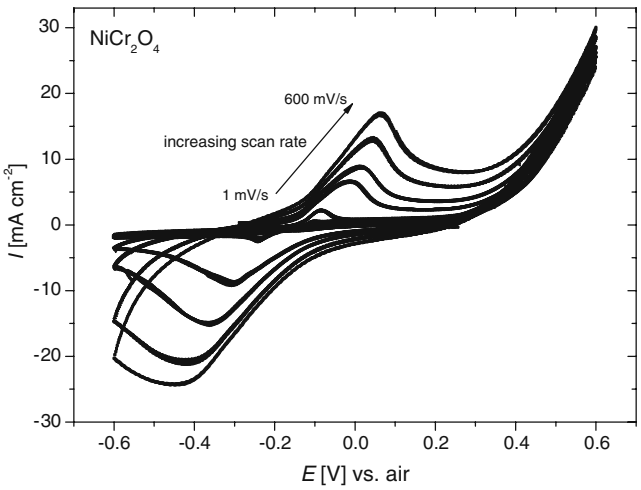

Fig. 10 CV on $NiCr_2O_4$ at 500 °C. Data were recorded in 1% NO using different sweep rates

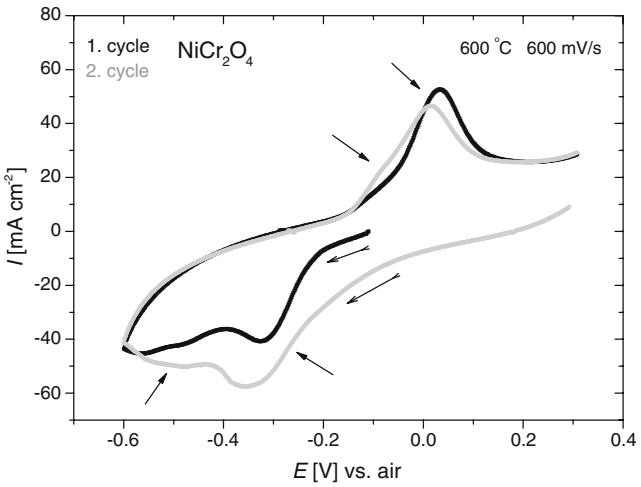

Fig. 11 Part of the cyclic voltammogram recorded at 600 °C (sweep rate: 600 mV s^{-1}). *Bold arrows* show the reduction/oxidation peaks, whereas the *thin peaks* show the direction of the scan

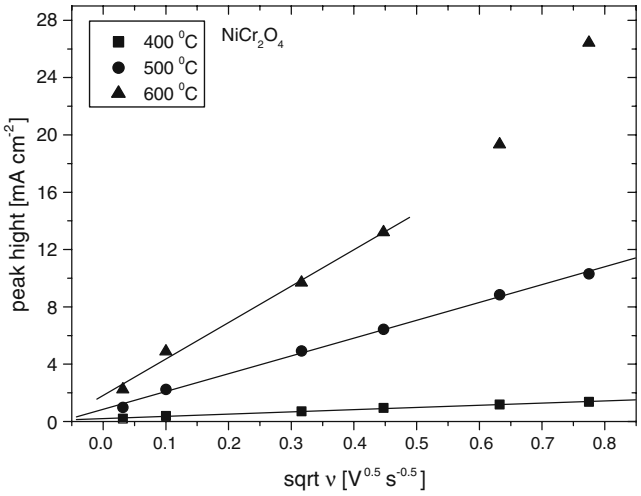

Fig. 12 Peak height plotted vs the square root of the sweep rate. A linear trend can be detected at 400 and 500 °C; however, at 600 °C, the linearity is disturbed at high sweep rates

fits, on the other hand, quite well with the oxidation of Cr, and it cannot be ruled out that it contributes to the peak formation.

Conclusion

Substitution of Fe^{3+} with Cr^{3+} in the spinel-type oxides; $NiCr_xFe_{2-x}O_4$ show a decrease of unit cell parameters and an increase of the conductivity. Dilatometry measurements show a decrease in the linear expansion in the measured temperature range and, in most samples, the Curie temperature and a cation redistribution could also be detected. CV and EIS were recorded on the spinels in 1% NO, 1% NO_2, and 10% O_2. Results show that the activity of $NiFe_2O_4$ is relatively high in NO and NO_2. However, it also has a high activity in O_2. The activity of $NiCr_2O_4$ is, although lower than for $NiFe_2O_4$, also relatively high. However, the activity in O_2 is low, which makes it a candidate for a possible electrode material in an electrochemical cell for the reduction of NO_x gases from a diesel fired engine. Formation of peaks in the voltammograms on the $NiCr_2O_4$ electrode suggests the formation of nitrogen-containing species on the surface or, alternatively, oxidation of Cr in the electrode.

References

1. Butler AR, Williams DLH (1993) Chem Soc Rev 22:233
2. Manahan SE (1994) Enviromental chemistry, 6th edn. CRC, London
3. Pancharatnam S, Huggins RA, Mason DM (1975) J Electrochem Soc 122:869
4. Gür T, Huggins R (1979) J Electrochem Soc 19:1067
5. Iwayama K, Wang X (1998) Appl Catal B 19:137
6. Hibino T (1995) J Appl Electrochem 25:203
7. Hibino T, Ushiki K, Kuwahara Y (1995) J Chem Soc Faraday Trans 91:1955
8. Hamamoto K, Fujishiro Y, Awano M (2007) J Electrochem Soc 154:F172
9. Hamamoto K, Fujishiro Y, Awano M (2006) J Electrochem Soc 153:D167
10. Simonsen VLE, Johnsen MM, Hansen KK (2007) Top Catal 45:131
11. Hansen KK (2007) Electrochem Commun 9:2721
12. Kammer Hansen K, Skou EM, Christensen H (2000) J Electrochem Soc 147:2007
13. Kammer Hansen K, Skou EM, Christensen H (2005) Solid State Ionics 176:915
14. Simonsen VLE, Nørskov L, Kammer Hansen K (2008) J Solid State Electrochem 12:1573
15. Changguan WF, Teraoka Y, Kagawa S (1996) Appl Catal B 8:217
16. Changguan WF, Teraoka Y, Kagawa S (1997) Appl Catal B 12:237
17. Shangguan WF, Teraoka Y, Kagawa S (1998) Appl Catal B 16:149
18. Haneda M, Kintaichi Y, Hamada H (2005) Appl Catal B 55:169-175
19. Drouet C, Alphonse P, Rousset A (2001) Appl Catal B 33:35
20. Chen L, Horiuchi T, Mori T (1999) Catal Lett 60:237
21. Fino D, Russo N, Saracco G, Specchia V (2006) J Catal 242:38
22. Simonsen VLE, Find D, Lilliedal M, Petersen R, Hansen KK, (2007) Top Catal 45:143
23. Hansen KK, Christensen H, Skou EM (2000) Ionics 6:340
24. Bræstrup F, Hansen KK (2008) J Solid State Electrochem. doi:10.1007/s1000800806539
25. Zhuiykov S, Nakano T, Kunimoto A, Yamazoe N, Miura N (2001) Electrochem Commun 3:97
26. West DL, Montgomery FC, Armstrong TR (2005) J Electrochem Soc 152:H74
27. Stranzenbach M, Gramckow E, Saruhan B (2007) Sens Actuators B 127:224
28. Hansen KK, Christensen H, Skou EM, Skaarup SV (2000) J Appl Electrochem 30:193
29. Fabry P, Kleitz M, Deportes C (1972) J Solid State Chem 5:1
30. Chick LA, Pederson LR, Maupin GD, Bates JL, Thomas LE, Exarhos GJ (1990) Mater Lett 10:6
31. Petříček V, Dusek M, Palatinus L (2000) Jana2000, The crystallographic computing system. Institute of Physics, Praha
32. Hansen KK, Vels Hansen K (2007) Solid State Ionics 178:1379
33. Bruggeman DAG (1935) Ann Phys 24:636
34. Newman J (1966) J Electrochem Soc 113:501
35. Wang WG, Barfod R, Larsen PH, Kammer K, Bentzen JJ, Hendriksen PV, Mogensen M (2003) In: Singhal SC, Dokiya M (ed) Solid oxide fuel cells VIII, vol 7. Electrochemical Society, Pennington
36. Klein C, Hurlbut CS, Dana JD (1998) Manual of mineralogy, 21th edn. Wiley, New York
37. Kedem D, Rothem T (1967) Phys Rev Lett 18:165
38. Bongers PF, Philips (1967) Tech Rev 28:13
39. Ata-Allah SS, Fayek MK, Yehia M (2004) J Magn Magn Mater 279:411

40. Ata-Allah SS, Sayedamed FM, Kaiser M, Hashhash AM (2005) J Mater Sci 40:2923
41. Yaresko A, Antonov V (2007) J Magn Magn Mater 310: 1672
42. Touloukian YS, Ho CY (1977) Thermophysical properties of matter. The TPRC data series vol 13. Plenum, New York
43. Rais A, Gismelseed AM, Al-Omari IA (2005) Phys Stat Sol B 242:1497
44. Redfern SAT (2002) Eur J Mineral 14:251
45. O'Bryan HM, DiMarcello FV (1970) J Am Ceram Soc 53:413
46. Dieckmann R, (1984) Solid State Ionics 12:1
47. Corbel G, Mestiri S, Lacorre P (2005) Solid State Sci 7:1216
48. COMSOL (2007) COMSOL version 3.4. www.comsol.com
49. Bard AJ, Faulkner LR (2001) Electrochemical methods, 2nd edn. Wiley, New York
50. Atkins P, de Paula J (2002) Atkins' physical chemistry, 7th edn. Oxford, Oxford
51. ThermFact (2007) FactSage version 5.5. www.factsage.com
52. Holcomb GR, Alman DE (2006) Scr Mater 54:1821
53. Machkova M, Zwetanova A, Kozhukharov V, Raicheva S (2008) J Uni Chem Tech Metall 43:53
54. Mikuli E, Migdał-Mikuli A, Chyży B, Grad B, Dziembaj R (2001) Thermochim Acta 370:65
55. Lide DR (2007) CRC Handbook of chemistry and physics, 87th edn. CRC, New York